A bi-potential contact formulation for recoverable adhesion between soft bodies based on the RCC interface model

L.B. Hu, Y. Cong, Pierre Joli, Zhi-Qiang Feng

▶ **To cite this version:**

L.B. Hu, Y. Cong, Pierre Joli, Zhi-Qiang Feng. A bi-potential contact formulation for recoverable adhesion between soft bodies based on the RCC interface model. Computer Methods in Applied Mechanics and Engineering, 2022, 390, pp.114478. 10.1016/j.cma.2021.114478 . hal-03481049

HAL Id: hal-03481049
https://hal.science/hal-03481049

Submitted on 15 Dec 2021

HAL is a multi-disciplinary open access archive for the deposit and dissemination of scientific research documents, whether they are published or not. The documents may come from teaching and research institutions in France or abroad, or from public or private research centers.

L'archive ouverte pluridisciplinaire **HAL**, est destinée au dépôt et à la diffusion de documents scientifiques de niveau recherche, publiés ou non, émanant des établissements d'enseignement et de recherche français ou étrangers, des laboratoires publics ou privés.

A bi-potential contact formulation for recoverable adhesion between soft bodies based on the RCC interface model

L.B. Hu [a], **Y. Cong** [a], **P. Joli** [a], **Z.-Q. Feng** [a,b, *]

[a] *Université Paris-Saclay, Univ Evry, LMEE, 91020, Evry, France*

[b] *School of Mechanics and Engineering, Southwest Jiaotong University, Chengdu, China*

Abstract

An extended, ready-to-implement 3D model for quasi-industrial problems of contact with friction and recoverable interface adhesion between soft material is formulated using the Raous-Cangémi-Cocou (RCC) interface model and a bi-potential based resolution method. According to the RCC description, the recoverable adhesive interface behaviour derives from a free surface energy and a surface dissipation pseudo-potential. The obtained interface law describes both the de-bonding process of adhesive links due to tangential and normal interface deformation, and reversely, the bonding process that takes place when two surfaces approach close enough. We then propose an associated formulation coupling 3D extended interface law and Blatz-Ko hyperelastic material, that enables modelling large deformations of foam type soft matters under conditions of contact and friction with recoverable adhesion. In the end, the subsequent local contact nonlinear equations are solved using a Newton-like algorithm within the bi-potential framework. Numerical examples are performed to demonstrate the capacity of the proposed approach.

Keywords: Dynamic contact; Adhesion; RCC model; Bi-potential method; Time-integration; Hyperelastic materials

1 Introduction

Dynamic frictional contact involving soft matters and recoverable interface adhesion represents a frequent phenomenon of contact. Widely observed in nature, with examples on both the macroscopic scale such as biological sticky pads of lizards and insects [1, 2], and the microscopic scale such as cell to cell contact [3, 4], recoverable adhesive contact has attracted significant attention in research, and inspired a variety of bio-mimetic applications [5–8].

In the area of numerical modelling, despite the efforts exerted over the last decade to develop adhesive contact algorithms [9–11], modelling realistic 3D problems of contact and friction with recoverable adhesion involving both bonding and de-bonding between soft matters, is still a challenging topic [12,13].

*Corresponding author.
E-mail address: zhiqiang.feng@univ-evry.fr

Accepted by Comp. Methods. in App. Mech. and Eng.
dec. 2021

Generally, describing such conditions of contact and friction requires developing appropriate 3D interface laws that reflect behaviours of the adhesive interface, and robust resolution algorithms that can tackle computational difficulties inherent to the contact non-linearity.

First, concerning the adhesive interface law, a number of models have been developed over the past decades. The most prominent ones include Johnson-Kendall-Roberts (JKR) [14], Maugis-Dugdale (MD) [15], and Greenwood and Johnson models [16]. These models, proposed as early as the 1970s and considered as reference in the area ever since, provided the theoretical basis for the contact and friction modelling of adhesive interfaces. Although these early models are limited to simple, normal-load scenarios, they inspired numerous subsequent researches that offer an extension to mixed-load schemes involving normal and tangential loads. We also note a few recent achievements based on finite element continuum contact models that incorporate mixed mode constitutive interface laws [13, 17, 18], all of which can describe the reaction of adhesive interfaces under complex load involving tension and shear. In this work, in order to simulate complex interface behaviours with reversible adhesion, we adopt the Raous-Cangémi-Cocou (RCC) model [19–22], which over the years has confirmed its robustness in dealing with adhesive frictional contact. The RCC model incorporates a complete set of interface law involving friction and reversible adhesion. It describes the strength of interface adhesion by prescribing an intensity parameter β [23]. Varying between 0 and 1, β characterizes the damage level of the interface adhesive bonds (0 refers to the state of complete de-bonding, 1 refers to complete bonding), and subsequently describes the reversible de-bonding and bonding process as function of the geometrical configuration of the contact interface [12, 24]. From a thermodynamic point of view, β derives from a free surface energy and a surface dissipation pseudo-potential. In this regard, the RCC interface model can be considered as a particular case of the unified adhesion interface model given in [25], which is similar to the Generalized Standard Material (GSM) [26] for material modelling. Here, based on 3D extension to the RCC model, a complete contact and friction law is formulated which leads to an extended Signorini condition and modified Coulomb friction rules.

The second aspect that requires attention is the severe non-linearities inherent to contact dynamics. In addition, the non-smooth and multivalued nature of the adhesive interface law gives rise to further computational difficulty. It is therefore necessary to apply robust, and stable algorithms to ensure iteration convergence, solution accuracy with balanced efficiency. General computational methods for numerical treatment of contact constraints include the penalty method [27], Lagrangian multiplier method [28] and augmented Lagrangian method [29,30]. In the current work, we propose to use the bi-potential theory which was developed based on the augmented Lagrangian method, and in the first place, to solve contact problems in the context of what is called implicit standard materials (ISM) [31, 32]. Compared to the traditional approach, the bi-potential method couples the two variational inequalities of the unilateral contact and friction law into one single displacement based variational principle with one unique inequality. Introduced in the 1990s, the approach has been recently extended to problems involving hyperelatic or elastic-to-plastic contact [33–35] with interface wear [36, 37]. In the area of adhesive contact modelling, the bi-potential theory has been recently applied to solve 2D interface adhesion between elastic materials [38]. Here, we extend its application to the context of 3D adhesive contact involving Blatz-Ko hyperelastic material [39] under the condition of large deformation.

By extending the RCC interface model, we aim to propose a ready-to-implement 3D formulation for solving quasi-industrial problems of adhesive contact with friction and recoverable interface between soft materials. The remaining content of the article is organized as follows: in Section 2, after a brief description of the contact kinematics, we present the complete framework of the adhesive contact law, which includes extended formulations of Signorini contact law and Coulomb friction rules. Then we present its implementation within the bipotential framework, and provide the formulation of the hyperelastic material used in this work. In Section 3, the complete finite element formulation of

the problem, including the resolution algorithm, is provided. To validate the framework, we present numerical examples in Section 4. In the end, a few concluding remarks are drawn in Section 5.

2 Problem setting

2.1 Contact kinematics

We describe in this section the geometric definitions and notations related to the contact kinematics. Let's consider two deformable bodies B^1 and B^2 coming into contact with N_c contact points. Each body is discretized with finite elements with nodal positions represented by $\mathbf{X}_1$ (for B^1) and $\mathbf{X}_2$ (for B^2) defined in the global coordinate system. Contact points belonging to B^1 are denoted by P_1^α ($\alpha = 1, 2, ...N_c$), and accordingly P_2^α. Positions of P_1^α and P_2^α can be written using an interpolation matrix $\mathbf{B}_1$ (accordingly $\mathbf{B}_2$) as:

$$\mathbf{X}(P_1^\alpha) = \mathbf{B}_1\mathbf{X}_1, \quad \mathbf{X}(P_2^\alpha) = \mathbf{B}_2\mathbf{X}_2. \tag{1}$$

We consider on each P_1^α a local orthogonal coordinate system, formed by $\mathbf{T}_1$, $\mathbf{T}_2$ and $\mathbf{N}$, representing respectively the tangential, and normal direction vectors defined with respect to the global coordinates. Therefore, P_1^α can be seen as the projection point of P_2^α on B^1. We can build the relative position between P_1^α and P_2^α by

$$\mathbf{X}^\alpha = \mathbf{X}(P_2^\alpha) - \mathbf{X}(P_1^\alpha), \tag{2}$$

with $\mathbf{X}(P_1^\alpha)$ and $\mathbf{X}(P_2^\alpha)$ the position vectors of P_1^α and P_2^α in the global coordinates. We can then introduce $\mathbf{x}^\alpha$, the local relative position vector of the contact point α, by projecting $\mathbf{X}^\alpha$ in the system $(\mathbf{T}_1, \mathbf{T}_2, \mathbf{N})$:

$$\mathbf{x}^\alpha = \left\{ \begin{array}{l} x_{t_1}^\alpha = \mathbf{T}_1^T\mathbf{X}^\alpha \\ x_{t_2}^\alpha = \mathbf{T}_2^T\mathbf{X}^\alpha \\ x_n^\alpha = \mathbf{N}^T\mathbf{X}^\alpha \end{array} \right\}. \tag{3}$$

We can thus express the local position vector $\mathbf{x}^\alpha$ as function of the global vector $\mathbf{X}$:

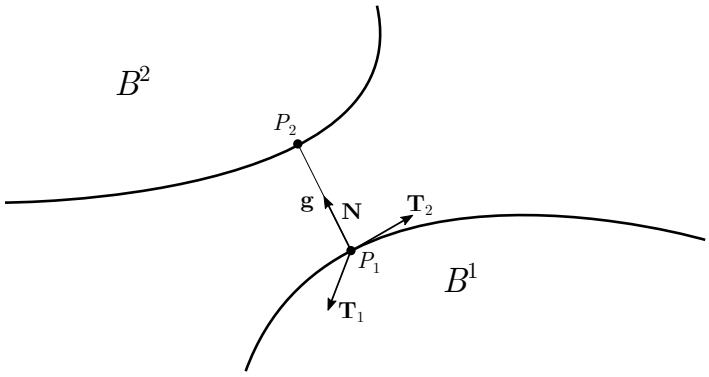

Figure 1: Contact kinematics

$$\mathbf{x}^\alpha = \mathbf{H}_\alpha\mathbf{X}^\alpha, \tag{4}$$

where $\mathbf{H}_\alpha$ is the transition matrix obtained by combining Eqs.(1,2,3). Similar relations can be determined with respect to contact forces. The local gap vector between two contact points can be derived

from the incremental form of Eq.(4):

$$\mathbf{x}_{i+1}^{\alpha} = \mathbf{H}_{\alpha}\Delta\mathbf{X}_{i}^{\alpha} + \mathbf{g}^{\alpha}, \tag{5}$$

with $\mathbf{g}^{\alpha} = (0, 0, g^{\alpha})^T$, the initial gap vector.

Then, let's denote the local and global contact force vectors with respectively $\mathbf{r}^{\alpha}$ and $\mathbf{R}^{\alpha}$. By writing the virtual work

$$(\mathbf{r}^{\alpha})^T\delta\mathbf{x}^{\alpha} = (\mathbf{R}^{\alpha})^T\delta\mathbf{X}^{\alpha}, \tag{6}$$

we obtain the relation between contact force vectors expressed in local and global coordinate systems:

$$\mathbf{R}^{\alpha} = \mathbf{H}_{\alpha}^{T}\mathbf{r}^{\alpha}. \tag{7}$$

Here, due to the presence of adhesion on the contact interface, contact reaction $\mathbf{r}^{\alpha}$ is composed of the cumulative effects due to both dry contact and the interface adhesion, hence

$$\mathbf{r}^{\alpha} = \bar{\mathbf{r}}^{\alpha} + \tilde{\mathbf{r}}^{\alpha}, \tag{8}$$

in which we use $\bar{\mathbf{r}}$ to denote dry contact reactions, and $\tilde{\mathbf{r}}$ contact forces due to interface adhesion. Note that the above relation can be projected to the local coordinate system according to the normal and tangential directions:

$$\begin{cases} r_n^{\alpha} = \bar{r}_n^{\alpha} + \tilde{r}_n^{\alpha} \\ \mathbf{r}_t^{\alpha} = \bar{\mathbf{r}}_t^{\alpha} + \tilde{\mathbf{r}}_t^{\alpha} \end{cases} . \tag{9}$$

We now assemble all the N_c contact points based on Eqs.(4,5,7), we obtain the following geometric and kinematic relations:

$$\begin{cases} \mathbf{x} = \mathbf{H}\Delta\mathbf{X} + \mathbf{g} \\ \mathbf{R} = \mathbf{H}^T\mathbf{r} \end{cases} , \tag{10}$$

with

$$\mathbf{H} = \begin{bmatrix} \mathbf{H}_1 \\ \vdots \\ \mathbf{H}_{N_c} \end{bmatrix}, \ \mathbf{x} = \begin{bmatrix} \mathbf{x}^1 \\ \vdots \\ \mathbf{x}^{N_c} \end{bmatrix}, \ \mathbf{r} = \begin{bmatrix} \bar{\mathbf{r}}^1 + \tilde{\mathbf{r}}^1 \\ \vdots \\ \bar{\mathbf{r}}^{N_c} + \tilde{\mathbf{r}}^{N_c} \end{bmatrix}, \ \mathbf{g} = \begin{bmatrix} \mathbf{g}^1 \\ \vdots \\ \mathbf{g}^{N_c} \end{bmatrix}. \tag{11}$$

2.2 RCC model for recoverable adhesion

We use in this work the RCC model to describe the effect of recoverable adhesion between contact surfaces introduced by Raous *et al.* [22], this model accounts for unilateral contact, friction and adhesion, based on an energy description of the contact interface, involving a free surface energy Ψ written as:

$$\Psi(\mathbf{x}_t, x_n, \beta) = \frac{C_n}{2}x_n^2\beta^2 + \frac{C_t}{2}\|\mathbf{x}_t\|^2\beta^2 - w\beta + \bigcup_{\Re+}(x_n) + \bigcup_{Q}(\beta) \quad , \tag{12}$$

and a pseudo-potential of the surface dissipation Φ:

$$\Phi(\dot{\mathbf{x}}_t, x_n, \dot{\beta}) = \mu|r_n - C_n x_n\beta^2|\|\dot{\mathbf{x}}_t\| + \frac{b}{2}|\dot{\beta}|^2 \quad . \tag{13}$$

In these expressions, β is a scalar parameter measuring the intensity of adhesion [23], with $\beta \in [0, 1]$. Specifically, $\beta = 0$ represents no adhesion, $\beta = 1$ indicates perfect adhesion. Therefore, any $\beta \in (0, 1)$ refers to partial adhesion between contact surfaces. Other parameters in Eqs.(12,13) include: C_t and C_n: parameters characterizing the initial adhesive stiffness when adhesion is complete, w: decohesion

energy threshold, $\bigcup$: indicator function that assures unilateral contact ($x_n \geqslant 0$), and meaningful values of the degree of adhesion. The subscript Q indicates $Q = \{\eta \mid 0 \leqslant \eta \leqslant 1\}$, μ: friction coefficient, b: surface viscosity.
Deriving the surface free energy Eq.(12), we obtain the expression of the normal force of adhesion:

$$r_n^{ad} = C_n x_n \beta^2 \ , \tag{14}$$

and the tangential force of adhesion:

$$\mathbf{r}_t^{ad} = C_t \mathbf{x}_t \beta^2 \ . \tag{15}$$

Both adhesion forces are dependent on the degree of adhesion β. Then deriving energy functions Eq.(12) and Eq.(13) with respect to β and $\dot{\beta}$ yields the incremental expression of β which gives its evolution in time:

$$\begin{cases} b\dot{\beta} \geq 0 & \text{with} \quad \beta = 0 \\ b\dot{\beta} = w - (C_n x_n^2 + C_t \|\mathbf{x}_t\|^2)\beta & \text{with} \quad 0 < \beta < 1 \\ b\dot{\beta} \leq w - (C_n x_n^2 + C_t \|\mathbf{x}_t\|^2) & \text{with} \quad \beta = 1 \quad . \end{cases} \tag{16}$$

In Eq.(16), we can see that two components may impact the variation of β: the decohesion energy w and the elastic energy of the interface. When interface elastic energy prevails, $\dot{\beta}$ becomes negative, leading to decreasing β. Otherwise, $\dot{\beta}$ is positive, then β increases. We can view this adhesive model as a special spring system whose elasticity incorporates damage and self-recoverable behaviours. In this regard, the value of β can be seen as the degree of damage of the spring, whose stiffness is adjustable based on β. Therefore, the decrease of the degree of adhesion β corresponds to the process of spring damage and breaking. Inversely, it can be seen as a recovering process of the spring stiffness.

2.3 Adhesive contact law and friction rule

2.3.1 Modified Signorini law with adhesion

We recall the unilateral contact law, also called Signorini law, which for classical dry contact is characterized by conditions of non-penetration and non adhesion. By using $\bar{r}_n^\alpha$ to denote local normal contact force on the point α due to dry contact, and the contact distance x_n, we have

$$\begin{cases} x_n^\alpha = \Delta x_n^\alpha + g = 0, & \bar{r}_n^\alpha \geqslant 0 \\ x_n^\alpha = \Delta x_n^\alpha + g > 0, & \bar{r}_n^\alpha = 0 \end{cases} \quad \Rightarrow \ x_n^\alpha \bar{r}_n^\alpha = 0 \ . \tag{17}$$

The first relation eliminates geometric penetration between contact surfaces. The second inequality indicates the absence of adhesion forces between dry contact surfaces once they are separated. For adhesive contact, since contact forces result from both the effects of dry contact and adhesion, the classical conditions of unilateral contact should be modified by considering Eq.(8), hence

$$\begin{cases} x_n^\alpha = 0, & r_n^\alpha - \tilde{r}_n^\alpha \geqslant 0 \\ x_n^\alpha > 0, & r_n^\alpha = \tilde{r}_n^\alpha \end{cases} \quad \Rightarrow \ x_n^\alpha (r_n^\alpha - \tilde{r}_n^\alpha) = 0 \ . \tag{18}$$

Here, adhesive forces $\tilde{r}_n^\alpha$ are zeros with surfaces in contact. They will appear when contact surfaces start to separate (the second relation), and $\tilde{r}_n^\alpha$ will tend to maintain the contact surfaces together. By considering Eq.(14), a modified Signorini condition with account for adhesion writes

$$\begin{cases} x_n^\alpha = 0, & r_n^\alpha - C_n x_n^\alpha \beta^2 \geqslant 0 \\ x_n^\alpha > 0, & r_n^\alpha = C_n x_n^\alpha \beta^2 \end{cases} \quad \Rightarrow \ x_n^\alpha (r_n^\alpha - C_n x_n^\alpha \beta^2) = 0 \ . \tag{19}$$

The obtained unilateral contact law that incorporates the effect of interface adhesion (Eq.(19)) can be graphically represented by Figure 2.

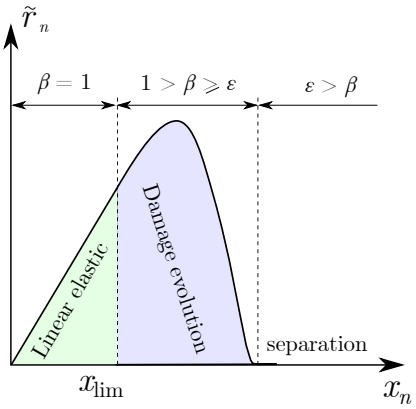

Figure 2: Modified Signorini law with adhesion: graphic representation of normal adhesion forces and the level of damage that evolves with contact distance. An empirical limit of β, denoted by ε, is adopted. With $\beta < \varepsilon$ ($\varepsilon = 10^{-4}$), adhesion bonds are considered broken.

By assuming perfect adhesion ($\beta = 1$) at $x_n = 0$, the state of interface adhesion that evolves with x_n can be distinguished by three major phases:

(i) **Fully bonded adhesion**: Adhesion bonds remain undamaged ($\beta = 1$). In this phase, elastic energy due to x_n does not exceed the decohesion threshold w. Hence, linear behaviour dominates the adhesion force *vs.* displacement curve (light green area in Figure 2).

(ii) **Adhesion with damage**: This phase is highlighted by the light cyan area in Figure 2. In this phase, β decreases as the decohesion energy w is overpassed. Damage starts to accumulate on adhesion bonds. Adhesion force $\tilde{r}_n^\alpha = C_n x_n^\alpha \beta^2$ continues to increase briefly with x_n, before it decreases under the effect of the decreasing quadratic term β^2, that represents the effect of damage to the interface adhesion.

(iii) **Separation**: Contact surfaces are separated due to broken adhesion bonds. β significantly decreases during the process. According to Eq.(16), the decreasing β only tends towards zero without exactly reaching zero. It is therefore convenient to consider a limit of β, that we denote by ε, below which the adhesion bonds can be considered as completely broken. In practice, we adopt an empirical $\varepsilon = 10^{-4}$ which is associated with adhesion forces on the 10^{-9} magnitude according to our tests (An example is provided in supplementary information).

2.3.2 Modified Coulomb friction rule with adhesion

Classically, friction problems are studied using the Coulomb friction model which is characterized by a set of rate-independent slip rules. It describes tangential contact forces as a function of normal forces in the context of dry friction:

$$\begin{cases} \|\bar{\mathbf{r}}_t^\alpha\| \leqslant \mu \bar{r}_n^\alpha & \forall \, \|\mathbf{x}_t^\alpha\| = 0 \quad \text{(sticking)} \\ \bar{\mathbf{r}}_t^\alpha = -\mu \bar{r}_n^\alpha \frac{\mathbf{x}_t^\alpha}{\|\mathbf{x}_t^\alpha\|} & \forall \, \|\mathbf{x}_t^\alpha\| \neq 0 \quad \text{(sliding)} \, . \end{cases} \tag{20}$$

Taking adhesion into consideration, both tangential and normal contact forces are supplemented by contributions due to interface adhesion as shown in Eq.(8), the above rules become

$$\begin{cases} \|\mathbf{r}_t^\alpha\| \leqslant \mu r_n^\alpha & \forall \, \|\mathbf{x}_t^\alpha\| = 0 \quad \text{(sticking)} \\ \mathbf{r}_t^\alpha = -\mu(r_n^\alpha - \tilde{r}_n^\alpha)\frac{\mathbf{x}_t^\alpha}{\|\mathbf{x}_t^\alpha\|} + \tilde{\mathbf{r}}_t^\alpha & \forall \, \|\mathbf{x}_t^\alpha\| \neq 0 \quad \text{(sliding)} \, , \end{cases} \tag{21}$$

in which $\tilde{\mathbf{r}}_t^\alpha$, the adhesive tangential force on contact point α can be calculated by considering Eq.(15):

$$\tilde{\mathbf{r}}_t^\alpha = -C_t \mathbf{x}_t^\alpha \beta^2 \, , \tag{22}$$

and in the normal direction, contact forces are

$$\begin{cases} r_n^\alpha - \tilde{r}_n^\alpha = \bar{r}_n^\alpha & \forall \, x_n^\alpha = 0 \quad \text{(unseparated)} \\ r_n^\alpha - \tilde{r}_n^\alpha = 0 & \forall \, x_n^\alpha > 0 \quad \text{(separated)} \, . \end{cases} \tag{23}$$

Taking interface adhesion into consideration, tangential friction is made from two contributions. The first follows the classical Coulomb rule and disappears once contact surfaces are separated. The second, $\tilde{\mathbf{r}}_t^\alpha$, the adhesive tangential force appears when slip occurs, and maintains even with the surface starting to separate.

The obtained rule of tangential contact with interface adhesion (Eqs.(21,22)) can be graphically interpreted by Figure 3. By assuming perfect adhesion ($\beta = 1$) at $x_t = 0$, the state of interface

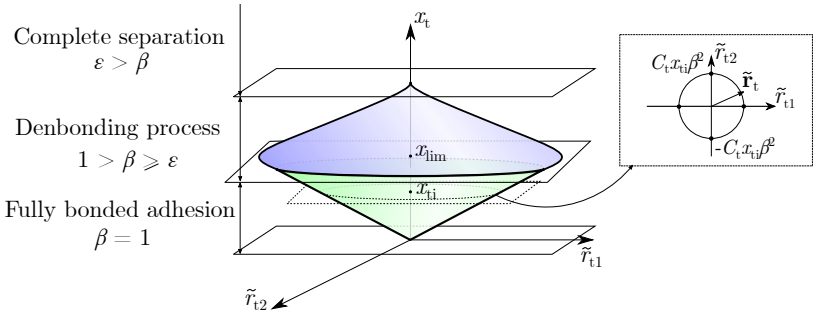

Figure 3: Modified Coulomb rule with adhesion: evolution of tangential adhesive forces and the level of damage *vs.* slip

adhesion that evolves with x_t can be distinguished, similar to the normal scenario described in the previous section, by three major phases: (i) fully bonded adhesion, (ii) adhesion with damage, and (iii) separation. Here, since both the slip vector $\mathbf{x}_t^\alpha$ and the tangential adhesion force vector $\tilde{\mathbf{r}}_t^\alpha$ lie in the local plane $(\mathbf{T}_1, \mathbf{T}_2)$, their projection in the local system gives rise to expressions of tangential displacement and forces according to axis $\mathbf{T}_1$ and $\mathbf{T}_2$. In the case of isotropic tangential behaviour, the adhesion stiffness can be described by a unique parameter C_t. Therefore, vectors of tangential forces lie on a circle of radius $C_t x_t \beta^2$. For any given slip value x_t, one distinct circle can be drawn, which graphically leads to a conic representation of the adhesion force by swiping x_t from 0 to $+\infty$ as shown in Figure 3.

2.3.3 Complete contact law with adhesion

By combining the modified Signorini law and Coulomb rule, we obtain the complete contact law with the account for interface adhesion as follows:

$$\begin{array}{lll} \text{Separation :} & x_n^\alpha > 0, & \mathbf{r}^\alpha = \tilde{\mathbf{r}}^\alpha \\ \text{Sticking :} & x_n^\alpha = 0 \text{ and } \|\mathbf{x}_t^\alpha\| = 0, & \mathbf{r}^\alpha = \bar{\mathbf{r}}^\alpha \\ \text{Sliding :} & x_n^\alpha = 0 \text{ and } \|\mathbf{x}_t^\alpha\| > 0, & \mathbf{r}_n^\alpha = \bar{\mathbf{r}}_n^\alpha \\ & & \mathbf{r}_t^\alpha = -\mu \bar{r}_n^\alpha \frac{\mathbf{x}_t^\alpha}{\|\mathbf{x}_t^\alpha\|} - C_t \mathbf{x}_t^\alpha \beta^2 \ , \end{array} \tag{24}$$

in which $\bar{\mathbf{r}}_n^\alpha$ refers to the normal contact force on point α when surfaces are in contact. In the Sticking situation, since no relative motion occurs, adhesive forces are absent, contact force vector $\bar{\mathbf{r}}^\alpha$ lies in the classical Coulomb cone $\mathbf{K}_\mu$, defined by

$$\mathbf{K}_\mu = \{\bar{\mathbf{r}}^\alpha \in \mathbb{R}^3 \mid \quad r_n^\alpha \geqslant 0, \ \|\mathbf{r}_t^\alpha\| - \mu r_n^\alpha \leqslant 0\}. \tag{25}$$

However, with the appearance of relative motion, either following the normal direction (Separation case), or the tangential direction (Sliding case), the contact force vector $\mathbf{r}^\alpha$ exceeds the boundary of the classical Coulomb cone $\mathbf{K}_\mu$ due to the adhesive forces $\tilde{\mathbf{r}}^\alpha$. Contrary to the classical Coulomb model for dry friction, the resultant contact force $\mathbf{r}^\alpha$ will not remain on the boundary of the Coulomb Cone since the relation between $\|\mathbf{r}_t^\alpha\|$ and r_n^α is no longer linear, but subject to variations due to evolving β, $\mathbf{x}_t^\alpha$ and x_n^α. We cannot conclude an explicit expression relating $\mathbf{r}$ to $\mathbf{x}$. In the work of Terfaya et al. [38], the adhesion is directly incorporated into the bipotential [32]. We have adopted a different approach where the progression of adhesion is solved at the resolution level by the augmented Lagrangian method, which offers as accurate results.

2.4 Contact law within the bipotential method

The bipotential function and inequality of contact law is as follows:

$$b_c(-\mathbf{x}^\alpha, \mathbf{r}^\alpha) = \bigcup_{\Re-}(-x_n^\alpha) + \bigcup_{\mathbf{K}_u}(\mathbf{r}^\alpha) + \mu r_n^\alpha || - \mathbf{x}_t^\alpha || \tag{26}$$

$$b_c(-\mathbf{x}^\alpha, \mathbf{r}'^\alpha) - b_c(-\mathbf{x}^\alpha, \mathbf{r}^\alpha) \geq -\mathbf{x}^\alpha \cdot (\mathbf{r}'^\alpha - \mathbf{r}^\alpha), \ \forall \ \mathbf{r}'^\alpha \in \mathbf{K}_\mu \ , \tag{27}$$

where $\bigcup$ is the indicator function. $\Re-$ and $\mathbf{K}_\mu$ represent respectively the negative real numbers and Coulomb cone.

The indicator functions become null when the variables $-\mathbf{x}^\alpha$ and $\mathbf{r}^\alpha$ comply with the restraining conditions.

We multiply both sides of the inequality (27) a parameter ρ, which is used to ensure numerical convergence, and substitude (26) into (27):

$$\rho\mu(r_n'^\alpha - r_n^\alpha)|| - \mathbf{x}_t^\alpha|| + [\mathbf{r}^\alpha - (\mathbf{r}^\alpha - \rho\mathbf{x}^\alpha)] \cdot (\mathbf{r}'^\alpha - \mathbf{r}^\alpha) \geq 0 \ . \tag{28}$$

Taking into account the decomposition $\mathbf{x} = \mathbf{x}_t + x_n\mathbf{n}$, the following inequality has to be satisfied:

$$(\mathbf{r}^\alpha - \mathbf{r}^{*\alpha}) \cdot (\mathbf{r}'^\alpha - \mathbf{r}^\alpha) \geq 0, \ \forall \ \mathbf{r}'^\alpha \in \mathbf{K}_\mu \ , \tag{29}$$

where the modified augmented contact force $\mathbf{r}^{*\alpha}$ is defined by:

$$\mathbf{r}^{*\alpha} = \mathbf{r}^\alpha - \rho(\mathbf{x} + \mu|| - \mathbf{x}_t^\alpha||\mathbf{n}) \ , \tag{30}$$

$\mathbf{r}^\alpha$ is the projection of $\mathbf{r}^{*\alpha}$ onto the closed convex Coulomb cone:

$$\mathbf{r}^\alpha = Proj(\mathbf{r}^{*\alpha}, \mathbf{K}_u) \ . \tag{31}$$

According to the three different contact states, the projection procedure becomes:

$$\begin{array}{lll} \text{if} & \mu||\mathbf{r}_t^{*\alpha}|| < -r_n^{*\alpha} \quad \text{then} \quad \mathbf{r}^{\alpha} = 0 & \text{separating} \\ \text{elseif} & ||\mathbf{r}_t^{*\alpha}|| \leq \mu r_n^{*\alpha} \quad \text{then} \quad \mathbf{r}^{\alpha} = \mathbf{r}^{*\alpha} & \text{sticking} \\ \text{else} & \mathbf{r}^{\alpha} = \mathbf{r}^{\alpha *} - (\frac{||\mathbf{r}_t^{\alpha *}|| - \mu r_n^{\alpha *}}{1+\mu^2})(\frac{\mathbf{r}_t^{\alpha *}}{||\mathbf{r}_t^{\alpha *}||} + \mu \mathbf{n}) & \text{sliding .} \end{array} \tag{32}$$

2.5 Blatz-Ko hyperelastic model for soft materials

Blatz-Ko hyperelastic model [39] is widely used to describe behaviours of compressible foam type soft materials. In practical situations, such materials undergo large deformations. To deal with the geometrical transformation with large deformation, we use the deformation gradient tensor $\mathbf{F}$ for the soft bodies in contact:

$$\mathbf{F} = \mathbf{I} + \nabla \mathbf{u}, \tag{33}$$

where $\mathbf{I}$ is the unity tensor and $\mathbf{u}$ the displacement vector. The right Cauchy-Green deformation tensor $\mathbf{C}$ is defined as $\mathbf{C} = \mathbf{F}^T\mathbf{F}$, and the Green-Lagrangian strain tensor $\mathbf{E} = \frac{1}{2}(\mathbf{C} - \mathbf{I})$. In the case of hyperelastic law, there exists a strain energy density function W which is a scale function of one of the strain tensors, whose derivative with respect to a strain component determines the corresponding stress component. This can be expressed by

$$\mathbf{S} = 2\frac{\partial W}{\partial \mathbf{C}}, \tag{34}$$

where $\mathbf{S}$ is the second Piola-Kirchhoff stress tensor. In the particular case of isotropic hyperelasticity [40], Eq.(34) can be written by

$$\mathbf{S} = 2\left[I_3\frac{\partial W}{\partial I_3}\mathbf{C}^{-1} + \left(\frac{\partial W}{\partial I_1} + I_1\frac{\partial W}{\partial I_2}\right)\mathbf{I} - \frac{\partial W}{\partial I_2}\mathbf{C}\right], \tag{35}$$

where I_i denotes the three invariants of the right Cauchy-Green deformation tensor $\mathbf{C}$:

$$I_1 = C_{ii};\ I_2 = (I_1^2 - C_{ij}C_{ij})/2;\ I_3 = det(\mathbf{C}). \tag{36}$$

The Blatz-Ko strain energy density function is given as follows:

$$W = \frac{G}{2}\left(\frac{I_2}{I_3} + 2\sqrt{I_3} - 5\right), \tag{37}$$

where G is the shear modulus. By deriving the energy density (37) with respect to the three invariants, we obtain

$$\frac{\partial W}{\partial I_1} = 0;\ \frac{\partial W}{\partial I_2} = \frac{G}{2I_3};\ \frac{\partial W}{\partial I_3} = \frac{G}{2}\left(-\frac{I_2}{I_3^2} + \frac{1}{\sqrt{I_3}}\right). \tag{38}$$

Reporting the result in the second Piola-Kirchhoff stress tensor (35) gives

$$\mathbf{S} = G\left(J\mathbf{C}^{-1} - \mathbf{C}^{-2}\right), \tag{39}$$

where $J = det(\mathbf{F})$, the Cauchy stress tensor $\boldsymbol{\sigma}$ is calculated from the second Piola-Kirchhoff stress tensor as follows:

$$\boldsymbol{\sigma} = \frac{1}{J}\mathbf{F}\mathbf{S}\mathbf{F}^T. \tag{40}$$

3 Numerical implementation

3.1 Finite element formulation of the nonlinear problem

Since contact between soft bodies involves treatment of nonlinear kinematic relations and hyperelastic constitutive models (Section 2.5), we formulate the nonlinear finite element problem within the framework of large deformations. In this work, we use Green-Lagrangian strain tensor $\mathbf{E}$ which comprises both linear and nonlinear terms, as a function of nodal displacements $\mathbf{u}$:

$$\mathbf{E} = \Big(\mathbf{B}_L + \frac{1}{2}\mathbf{B}_{NL}(\mathbf{u})\Big)\mathbf{u}, \tag{41}$$

where $\mathbf{B}_L$ is the matrix relating the linear strain term to nodal displacements, and $\mathbf{B}_{NL}(\mathbf{u})$, relates the nonlinear strain term to nodal displacements. From Eq.(41), the incremental form of the strain-displacement relationship can be written as:

$$\delta\mathbf{E} = \big(\mathbf{B}_L + \mathbf{B}_{NL}(\mathbf{u})\big)\delta\mathbf{u}. \tag{42}$$

Using the principle of virtual displacement, we can write the virtual work δU of the problem as:

$$\delta U = \delta\mathbf{u}^T\mathbf{M}\ddot{\mathbf{u}} + \delta\mathbf{u}^T\mathbf{A}\dot{\mathbf{u}} + \int_{V_0} \delta\mathbf{E}^T\mathbf{S}\, dV - \delta\mathbf{u}^T\mathbf{F}_{ext} - \delta\mathbf{u}^T\mathbf{R} = 0, \tag{43}$$

where the second Piola-Kirchhoff stress tensor $\mathbf{S}$, in the case of Blatz-Ko material model is given in Section 2.5 by Eq.(39). The vector of contact reaction force $\mathbf{R}$ is expressed in the global coordinate system. It is obtained by considering Eqs.(7,8,10) and includes in particular contributions due to adhesion:

$$\mathbf{R} = \mathbf{H}^T(\bar{\mathbf{r}} + \tilde{\mathbf{r}}), \tag{44}$$

with $\bar{\mathbf{r}}$ and $\tilde{\mathbf{r}}$ determined according to the contact and friction rules given in Section 2.3. Other notations in Eq.(43) include V_0, volume of the initial configuration; $\mathbf{F}_{ext}$, vector of external loads; $\mathbf{M}$, mass matrix; $\mathbf{A}$, damping matrix; $\dot{\mathbf{u}}$, vector of velocity, and $\ddot{\mathbf{u}}$, vector of acceleration. Substituting $\delta\mathbf{E}$ from Eq.(42) into Eq.(43) results in

$$\delta U = \delta\mathbf{u}^T\mathbf{M}\ddot{\mathbf{u}} + \delta\mathbf{u}^T\mathbf{A}\dot{\mathbf{u}} + \delta\mathbf{u}^T\int_{V_0} \big(\mathbf{B}_L + \mathbf{B}_{NL}(\mathbf{u})\big)^T\mathbf{S}\, dV - \delta\mathbf{u}^T\mathbf{F}_{ext} - \delta\mathbf{u}^T\mathbf{R} = 0. \tag{45}$$

We can identify in Eq.(45) the vector of internal force:

$$\mathbf{F}_{int} = \int_{V_0} \big(\mathbf{B}_L + \mathbf{B}_{NL}(\mathbf{u})\big)^T\mathbf{S}dV. \tag{46}$$

Since $\delta\mathbf{u}$ is arbitrary, a set of nonlinear equations can be obtained as

$$\mathbf{M}\ddot{\mathbf{u}} + \mathbf{A}\dot{\mathbf{u}} + \mathbf{F}_{int} - \mathbf{F}_{ext} - \mathbf{R} = 0. \tag{47}$$

It is noted that the stiffness effect is taken into account by the internal force vector $\mathbf{F}_{int}$. Eq.(47) can be transformed into

$$\mathbf{M}\,\ddot{\mathbf{u}} = \mathbf{F} + \mathbf{R}, \quad \text{where} \quad \mathbf{F} = \mathbf{F}_{ext} - \mathbf{F}_{int} - \mathbf{A}\dot{\mathbf{u}}, \tag{48}$$

with the initial conditions at $t = 0$

$$\dot{\mathbf{u}} = \dot{\mathbf{u}}_0 \text{ and } \mathbf{u} = \mathbf{u}_0. \tag{49}$$

Taking the derivative of $\mathbf{F}_{int}$ with respect to the nodal displacements $\mathbf{u}$ gives the tangent stiffness matrix as

$$\mathbf{K} = \frac{\partial \mathbf{F}_{int}}{\partial \mathbf{u}} = \int_{V_0} \Big[\big(\mathbf{B}_L + \mathbf{B}_{NL}(\mathbf{u})\big)^T \frac{\partial \mathbf{S}}{\partial \mathbf{u}} + \frac{\partial \mathbf{B}_{NL}^T(\mathbf{u})}{\partial \mathbf{u}} \mathbf{S} \Big] dV. \tag{50}$$

In addition, by considering Eqs.(42, 39), the tangent stiffness matrix can be written as the sum of the elastic stiffness matrix $\mathbf{K}_e$, the geometric stiffness (or initial stress stiffness) matrix $\mathbf{K}_\sigma$ and the initial displacement stiffness matrix $\mathbf{K}_u$:

$$\mathbf{K} = \mathbf{K}_e + \mathbf{K}_\sigma + \mathbf{K}_u, \tag{51}$$

with

$$\begin{aligned} \mathbf{K}_e &= \int_{V_0} \mathbf{B}_L^T \mathbf{D} \mathbf{B}_L \, dV \\ \mathbf{K}_\sigma &= \int_{V_0} \frac{\partial \mathbf{B}_{NL}^T}{\partial \mathbf{u}} \mathbf{S} \, dV \\ \mathbf{K}_u &= \int_{V_0} \big(\mathbf{B}_L^T \mathbf{D} \mathbf{B}_{NL} + \mathbf{B}_{NL}^T \mathbf{D} \mathbf{B}_L + \mathbf{B}_{NL}^T \mathbf{D} \mathbf{B}_{NL} \big) dV. \end{aligned} \tag{52}$$

3.2 Numerical integration algorithm

Now we need to integrate Eq.(48) between consecutive time configuration t and $t + \Delta t$. The Newmark method is the most common method which is based on a second order algorithm. However, higher order approximation does not necessarily mean better accuracy and may even be redundant in impact problems. In cases presenting sudden change of contact conditions (impact, release of contact), we observe discontinuous velocity and acceleration, which lead to excessive regularity constraints that may cause serious errors. For this reason, we use the method of Non-Smooth Contact Dynamics (NSCD) [41] involving a first order time stepping algorithm. Implementation of this algorithm for adhesion problems has been investigated in [42]. Based on NSCD, Eq.(48) can be transformed into:

$$\mathbf{M}\, d\dot{\mathbf{u}} = \mathbf{F}\, dt + \mathbf{R}\, dt \ . \tag{53}$$

This algorithm is based on the following approximations:

$$\int_t^{t+\Delta t} \mathbf{M}\, d\dot{\mathbf{u}} = \mathbf{M} \left(\dot{\mathbf{u}}^{t+\Delta t} - \dot{\mathbf{u}}^t \right) \tag{54}$$

$$\int_t^{t+\Delta t} \mathbf{F}\, dt = \Delta t \left((1-\xi)\, \mathbf{F}^t + \xi\, \mathbf{F}^{t+\Delta t} \right) \tag{55}$$

$$\int_t^{t+\Delta t} \mathbf{R}\, dt = \Delta t\, \mathbf{R}^{t+\Delta t} \tag{56}$$

$$\mathbf{u}^{t+\Delta t} - \mathbf{u}^t = \Delta t \left[(1-\theta)\, \dot{\mathbf{u}}^t + \theta\, \dot{\mathbf{u}}^{t+\Delta t} \right] \ , \tag{57}$$

where $0 \le \xi \le 1$; $0 \le \theta \le 1$. In the iterative solution procedure, all the values at time $t+\Delta t$ are replaced by the values of the current iteration $i+1$; for example, $\mathbf{F}^{t+\Delta t} = \mathbf{F}^{i+1}$. A standard approximation of $\mathbf{F}^{i+1}$ gives

$$\mathbf{F}^{i+1} = \mathbf{F}_{int}^i + \frac{\partial \mathbf{F}}{\partial \mathbf{u}} (\mathbf{u}^{i+1} - \mathbf{u}^i) + \frac{\partial \mathbf{F}}{\partial \dot{\mathbf{u}}} (\dot{\mathbf{u}}^{i+1} - \dot{\mathbf{u}}^i) = \mathbf{F}_{int}^i - \mathbf{K}^i\, \Delta \mathbf{u} - \mathbf{A}^i\, \Delta \dot{\mathbf{u}} \ . \tag{58}$$

Finally, we obtain the recursive form of (53) in terms of displacements:

$$\boxed{\begin{array}{rl} \bar{\mathbf{K}}^i \, \Delta \mathbf{u} & = \bar{\mathbf{F}}^i + \bar{\mathbf{F}}^i_{acc} + \mathbf{R}^{i+1} \\ \mathbf{u}^{i+1} & = \mathbf{u}^i + \Delta \mathbf{u} \ , \end{array}} \tag{59}$$

where the so-called effective terms are given by

$$\bar{\mathbf{K}}^i = \xi \, \mathbf{K}^i + \frac{\xi}{\theta \, \Delta t} \mathbf{A}^i + \frac{1}{\theta \, \Delta t^2} \mathbf{M}^i \tag{60}$$

$$\bar{\mathbf{F}}^i_{acc} = -\frac{1}{\theta \Delta t^2} \, \mathbf{M}^i (\mathbf{u}^i - \mathbf{u}^t - \Delta t \, \dot{\mathbf{u}}^t) \tag{61}$$

$$\bar{\mathbf{F}}^i = (1 - \xi) \left(\mathbf{F}^t_{int} + \mathbf{F}^t_{ext} \right) + \xi \left(\mathbf{F}^i_{int} + \mathbf{F}^{t+\Delta t}_{ext} \right) \ . \tag{62}$$

At the end of each time step, the velocity is updated by

$$\dot{\mathbf{u}}^{t+\Delta t} = \left(1 - \frac{1}{\theta} \right) \dot{\mathbf{u}}^t + \frac{1}{\theta \, \Delta t} (\mathbf{u}^{t+\Delta t} - \mathbf{u}^t) \ . \tag{63}$$

By setting $\theta = \frac{1}{2}$, this scheme is then called the implicit trapezoidal rule and it is equivalent to the Tamma - Namburu method in which the acceleration need not be computed [43].

It is noted that Eq.(59) is strongly non-linear, because of large rotations and large displacements of solid, for instance in multibody contact/impact problems. Besides, as mentioned above, the constitutive law of contact with friction is usually represented by inequalities and the contact potential is even non differentiable. Instead of solving this equation in consideration of all nonlinearities at the same time, Feng [44] has proposed a solution strategy which consists in separating the nonlinearities in order to overcome the complexity of calculation and to improve the numerical stability. As $\Delta \mathbf{u}$ and $\mathbf{R}$ are both unknown, Eq.(59) cannot be directly solved. First, the vector $\mathbf{R}$ is determined by the bi-potential method and the adhesive model in a reduced system, which only concerns contact nodes. Then, the vector $\Delta \mathbf{u}$ can be computed in the whole structure, using adhesive contact reactions as external loading.

The iterative solution procedure involving contact modeling is written as Figure 4:

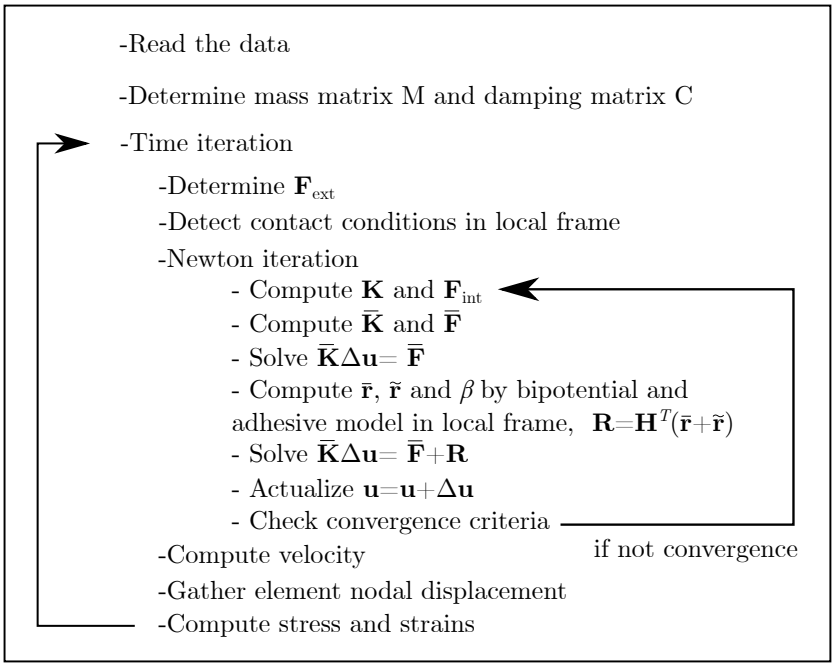

Figure 4: The iterative solution procedure

4 Numerical results

The algorithm presented above has been implemented within the in-house finite element code FER/Contact. In this section, four numerical examples based on contact simulations are presented to show normal and tangential behaviours of the adhesive contact interface under unidirectional and mixed loading conditions.

4.1 Indentation on adhesive hyperelastic material

The adhesion effect is usually most significant in the normal direction. In order to clearly show the evolution of β during the complete process of bonding and de-bonding, the first example simulates the normal adhesive contact between an elastic semi-sphere and a hyperelastic block, shown in Figure 5(a). The density of two bodies is: $\rho = 2500$ kg/m^{-3} (sphere indentor); $\rho = 1000$ kg/m^{-3} (block). Blatz-Ko hyperelastic material model is used and the shear modulus G for the indentor and the hyperelastic block are respectively 2.6×10^{10} Pa and 16×10^6 Pa. In this case, the sphere indentor behaves as a rigid body compared to the block.

A time dependent displacement is prescribed on the upper surface of the semi-sphere, so that a complete cycle of indentation is performed in 4 seconds. Figure 5(b) is the load curve showing the displacement of the upper surface of the sphere.

Figure 6(e) lists three different sets of adhesive parameters used in the test, whose results are reported in Figure 6(c). Cocou *et al.* investigated similar scenarios and obtained concordant results [12]. Figure 6(a) shows the evolution of β on 7 contact nodes in Case 1. On any contact point, its horizontal distance from the center point O determines the time length of the contact process on this point, involving bonding and de-bonding. The sequence of β evolution is thus distinctive on each point.

Figure 6(b) shows the normal adhesion force of the 7 contact nodes in Case 1. Similarly, the distance from the center point O determines the sequence of separation, which however does not influence the adhesion force at the moment of separation. Figure 6(c) shows evolution of β on the contact point A

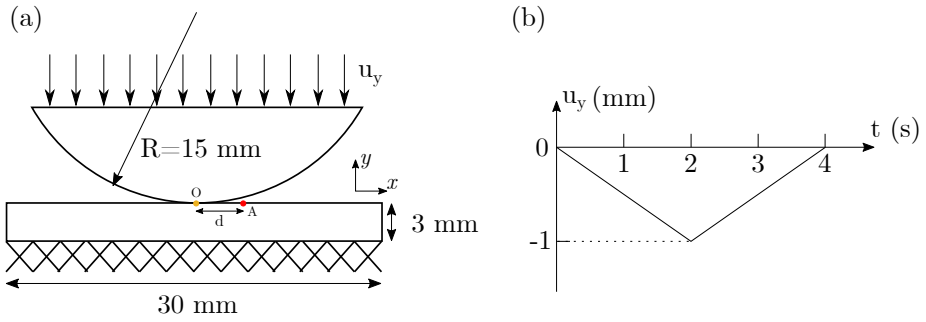

Figure 5: Indentation on a hyperelastic material with adhesive surface: (a) Problem set; (b) Loaded displacement on the upper surface of the sphere.

under 3 groups of different adhesive parameters. Figure 6(d) shows the normal adhesion force of the contact point A during the de-bonding process under 3 cases. We can see that the increase of C_n makes the detachment difficult. The difference in adhesion force determines the rate of decrease of β as shown in Figure 6(c).

4.2 Rolling adhesion of a hyperelastic wheel

This example investigates the rolling adhesion of a hyperelastic wheel confined between 2 rigid plates. As shown in Figure 7(a), the upper and lower plates exert compression on the hyperelastic wheel, and slide simultaneously in opposite directions, driving the wheel in rotation under both the effects of interface adhesion and friction. As a result of the interface adhesion, the rotating wheel presents inclined, asymmetrical geometry during rotation. Since the rotating motion is cyclic, any point belonging to the wheel's adhesive surface will cyclically go through bonding and de-bonding process. The recoverability of interface adhesion is thus accounted for. The present case follows the next loading sequence: the upper plate first descends vertically for 5×10^{-4} m at the velocity of 0.1 m/s, exerting slight compression on the wheel. Then, still on the upper plate, we prescribe a sliding motion at the velocity of 1 m/s so as to drive the compressed wheel in rotation. We investigate the effect of material properties on the adhesion by testing 3 different shear modulus $G = 5 \times 10^6$ Pa, 1×10^7 Pa, and 1.5×10^7 Pa for the hyperelastic wheel. Concerning the interface properties, the following parameters are used: friction coefficient $\mu = 0.4$. Note that setting non-zero friction here is important to drive the wheel to rotate. The wheel rotates consequently under the combined effects of interface friction and adhesion. Parameters for the adhesive are : $w = 20$ J.m^{-2}, $C_n = C_t = 2 \times 10^9$ N.m^{-3}, and $b = 0.1$ N.s.m^{-1}.

Figure 7(c) shows the morphology and Von Mises stress distribution of the hyperelastic wheel just following application of the compression by the upper plate. Figure 7(d) shows the state of deformation and Von Mises stress distribution of the wheel during its rotation. Due to the combined effects of the interface friction, which exerts pure tangential force on the wheel, and the interface adhesion, which results in both normal and tangential forces on the wheel surface, the rotating wheel deforms into inclined, asymmetrical geometry. This morphology is the result of the adhesion force (attraction) that appears at the separation (de-bonding) between the plate and the wheel. In case adhesion is absent and under the exclusive effect of friction, the wheel will not present inclined shape during rotation, but remain in the configuration of Figure 7(c).

Figure 8(a) shows the evolution of the adhesion parameter β, and the adhesion forces calculated on 3 selected nodes as indicated in Figure 7(b) with shear modulus $G = 1 \times 10^7$ Pa. The de-bonding sequence is consistent with the wheel's rotation direction. Figure 8(b) presents the evolution of β calculated on the first node (among the three selected nodes) under the 3 tested hyperelastic materials

(shear modulus $G = 5 \times 10^6$ Pa, 1×10^7 Pa, and 1.5×10^7 Pa). We demonstrate that material shear modulus has no effect on β during the bonding process, since the 3 curves perfectly coincide on this segment. However, during the de-bonding process, greater shear modulus accelerates the rupture of the adhesive bonds, which is obvious since stiffer material deforms less, and gets detached more easily from the plate during the prescribed rotation. The same observation is obtained on the normal adhesion force curves (Figure 8(c) and (d)).

4.3 Adhesive friction between a hyperelastic plate and a deformable semi-cylinder

In this example, we investigate the adhesive friction of a hyperelastic plate that slides on top of a deformable semi-cylinder, as shown in Figure 9(a). Both the plate and the semi-cylinder are modelled by Blatz-Ko hyperelastic material, based on the same material property with shear modulus $G = 10$ MPa. Radius of the cylinder is 5 mm, and the plate thickness $H = 2$ mm. The plate is sufficiently long so as to ensure contact between the plate and the cylinder during the simulation. While the plate is allowed to slide horizontally, the bottom surface of the semi-cylinder is fixed. The simulated scenario involves 2 stages. On the first stage, the upper plate descends for 1 mm to exert a slight compression on the cylinder. Then on the second stage, a lateral displacement is prescribed on the plate at a constant velocity. As a result of the combined effect of friction and adhesion, the cylinder is dragged to deform, and we investigate the interfacial behaviour during the process. In particular, by varying the descent velocity of the first stage, we modulate the total time of compression before sliding, during which the bonding process takes place. This will have impact on the final adhesion level (characterized by β) before de-bonding starts at the onset of the sliding stage. In order to explore the influence of the adhesion level β on the subsequent adhesive friction behaviour, we set up 5 groups of cases with for each group a different descent velocity (summarized by Figure 10(a)). Then for each group, we test on 5 different friction coefficients μ, so as to investigate the combined effect of friction and adhesion on the tangential interface behaviour. The adhesive parameters used in the simulations are: $w = 20$ J.m^{-2}, $C_n = 2 \times 10^9$ N.m^{-3} and $b = 0.1$ N.s.m^{-1}.

Figure 9(b) and (c) present the Von Mises stress distributions of the sliding system, respectively at the onset of sliding, and during the sliding process. We post-process the frictional adhesive behaviour by isolating 2 nodes belonging to the system: as seen in Figure 9(a), one blue node on the lower surface of the plate in contact with the cylinder, and one red node on top of the cylinder, in contact with the plate. Here, we investigate the evolution of β during the first stage. By considering different descent velocities of the plate, varying from 1000 mm/s to 200 mm/s, we modulate for each case the time for the bonding process. As shown in Figure 10(c), the case with the plate slowly descending at 200 mm/s (green curve) had sufficient time to achieve perfect bonding of adhesive links (β reached 1), whereas the most rapid descent (blue curve) did not allow enough time for the formation of complete bonding. In this case, de-bonding was already initiated after β reached 0.2. We then investigate the influence of friction coefficient μ on the de-bonding behaviour, by prescribing varying friction coefficients μ while considering the same plate descent velocity. We report in Figure 10(b) 5 simulations based on 5 values of μ ranging from 0 to 0.8. All the 5 cases consider the same plate descent velocity of 1000 mm/s (Case 1 of Figure 10(a)). Results in Figure 10(b) indicate the formation of stronger bond (higher β) on rougher surfaces (greater μ). This can be interpreted by the fact that a rougher surface (higher μ) delays the onset of sliding motion, according to the Coulomb friction model, which results in longer time for better bonding of adhesive links. Therefore, we observe a concordant trend on the curves reflecting tangential adhesion forces. With a greater friction coefficient (Figure 10(d)), the onset of de-bonding

is delayed, creating increased level of adhesion force. Then, lower descent velocity on the first stage (Figure 10(e)) also creates the effect of delaying the onset of de-bonding, permitting better bonding and more significant adhesion forces.

4.4 3D frictional adhesive twisting

We investigate the evolution of interface behaviours of a 3D twist tribosystem (Figure 11) under the combined effect of adhesion and friction. The system is composed of an elastomer block that slides on a rigid surface under twisting load. The elastomer block is 3 mm high, and has a 10×10 mm square section. The adhesive interface parameters are : $w = 100$ J.m^{-2}, $C_n = 2 \times 10^{10}$ N.m^{-3} and $b = 0.1$ N.s.m^{-1}. The simulation scenario involves 2 stages. On the first stage, we prescribe a slight compression on the elastomer by descending its upper surface by 0.1 mm. Then at the second stage, a twisting motion is applied on the upper surface at the angular velocity of 20 rad/s so as to drive the compressed elastomer block in clockwise twisting. The elastomer is modelled using Blatz-Ko material. To prevent excessive shear deformation of the elastomer body during the twist, we apply a significant shear modulus $G = 2.1 \times 10^6$ MPa.

We first investigate the effect of interface adhesion on the friction behaviour by comparing 2 test cases, one based on dry friction twist, the other involves friction with adhesion. Figure 12 compares the normal reaction forces of the two cases during the twist process. 9 frames of results are extracted in chronological order to represent the evolving twist process. On each frame, we compare distributions of the normal force calculated on the contact interface between dry friction and adhesive friction. Since the combined motion of compressive twisting is prescribed on the upper surface of the elastomer, the elastomer body undergoes shear deformation during the twist. On each side of the elastomer body, and along the direction of motion, the shearing kinematics creates a rotating moment that tends to press the frontal part of the body against the ground surface while detaching the rear part. This results in the evolving normal force distribution shown in Figure 12, where the increasing blue colour reveals local interface detachment, and the red colour indicates increased local compression. This phenomenon significantly increases with the interface adhesion, which becomes the prevailing source of resistance to the prescribed twist motion. Compared to the case of dry friction, interface sliding remains unnoticeable up to $t = 0.007$ s on the adhesive case: contact interface appears untwisted despite the external load, implying unbroken adhesive bonds. On the contrary, the dry friction interface is easily twisted by the external load, and the normal force distribution appears more homogeneous throughout the simulation. In this example, we observed initiation of de-bonding at $t = 0.007$ s ~ 0.008 s where normal forces decreased significantly, and the contact interface twisting quickly caught up with the dry friction case. Upon complete de-bonding, as can be seen in the frame $t = 0.009$ s, both cases present consistent configuration, with synchronized twists and similar distribution of normal forces.

We then explore the effect of friction coefficients on the combined adhesive-frictional interface behaviour, which includes interface forces and adhesion strength. Using 3 sets of friction coefficients $\mu = 0.2$, 0.4 and 0.6, we carry out simulations based on the previous adhesive tribosystem, and investigate, for each friction coefficient, the evolution of normal and tangential reactions, and the intensity of adhesion (represented by β). Figure 13 presents the distribution of normal contact forces that evolve with time for the tested 3 friction coefficients. Results obtained are concordant with what can be predicted by the Coulomb friction model, since under equivalent conditions of compression, stronger friction coefficients will have the effect of delaying the onset of interface sliding, and subsequently the initiation of the de-bonding process. For the same reason since the elastomer block admitted higher shear deformation before complete de-bonding, increased level of normal forces are observed on cases with higher friction coefficients. The effect of higher friction coefficients on the de-bonding process can be further confirmed

by investigating the evolution of β, as shown in Figure 14, in which the light yellow colour indicates the state of complete bonding of interface adhesives. We observe directly that higher friction coefficients significantly delay the onset of the de-bonding process.

We also investigate the evolution of tangential forces on the 3 sets of simulations. In Figure 15, Euclidean norm of tangential forces are presented, allowing us to observe the evolving intensity of tangential forces on the contact interface. In this figure, similar distribution of tangential forces can be observed on frames $\mu = 0.2$ / $t = 0.006$ s, $\mu = 0.4$ / $t = 0.007$ s, and $\mu = 0.6$ / $t = 0.008$ s, then, on frames $\mu = 0.2$ / $t = 0.007$ s, $\mu = 0.4$ / $t = 0.008$ s, and $\mu = 0.6$ / $t = 0.009$ s, and so on. This observation also results from the effect of higher friction coefficients on delaying the onset of be-bonding process, and subsequently the appearance of every distribution pattern of tangential forces. Chronologically, at the beginning of loading, tangential forces are most significant on the outskirts of the contact area since linear velocity is higher. However, for the same reason, this is also where the onset of de-bonding initiates and propagates towards the centre area. Consequently, the peak of tangential forces is observed as an evolving circular band, whose radius decreases with the twisting load, before it gradually disappears in the centre of rotation, leading to complete de-bonding of interface adhesives.

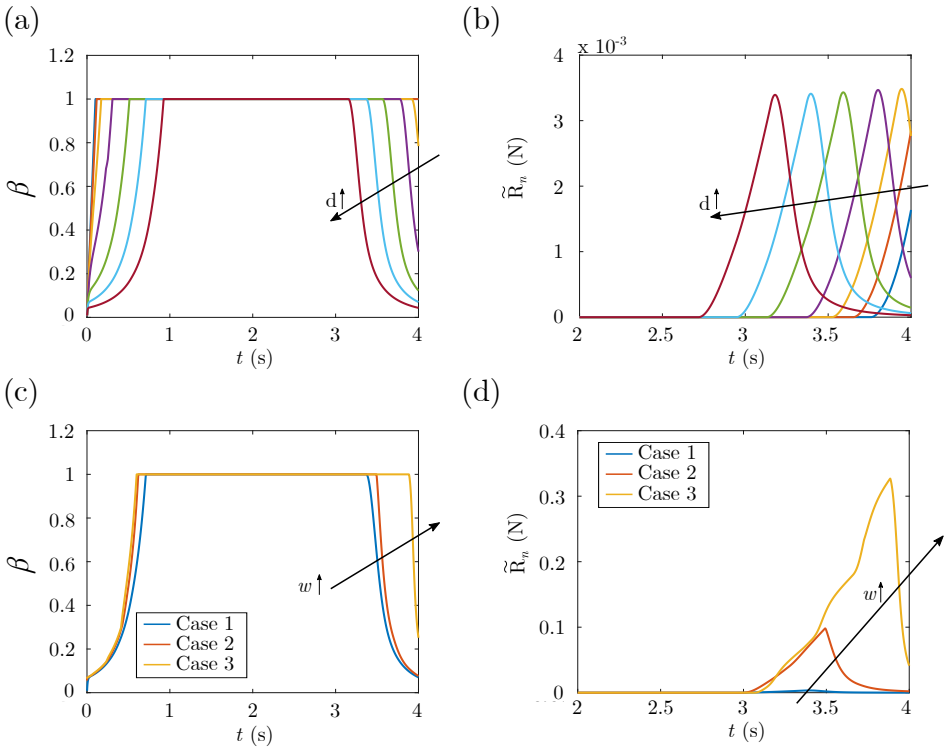

(e)

	w (J.m^{-2})	C_n(N.m^{-3})	b (N.s.m^{-1})
Case 1	1	1×10^{8}	0.1
Case 2	30	3×10^{9}	0.1
Case 3	100	1×10^{10}	0.1

Figure 6: Indentation on a hyperelastic material with adhesive surface: (a) Evolution of β calculated on 7 contact nodes of the hyperelastic block. At $t = 0$ s, the only contact point between the indentor and the block is point O, see Figure 5(a), and d represents the horizontal distance between each node and the center point O; (b) Evolution of the adhesion force $\tilde{\mathrm{R}}_n$ calculated on 7 contact nodes of the hyperelastic block; (c) Evolution of β with 3 different sets of adhesive parameters (w and C_n) on node A ($d = 3.4$ mm); (d) Evolution of the adhesion force $\tilde{\mathrm{R}}_n$ based on 3 different sets of adhesive parameters, calculated on node A; (e) Table of the tested adhesive parameter sets.

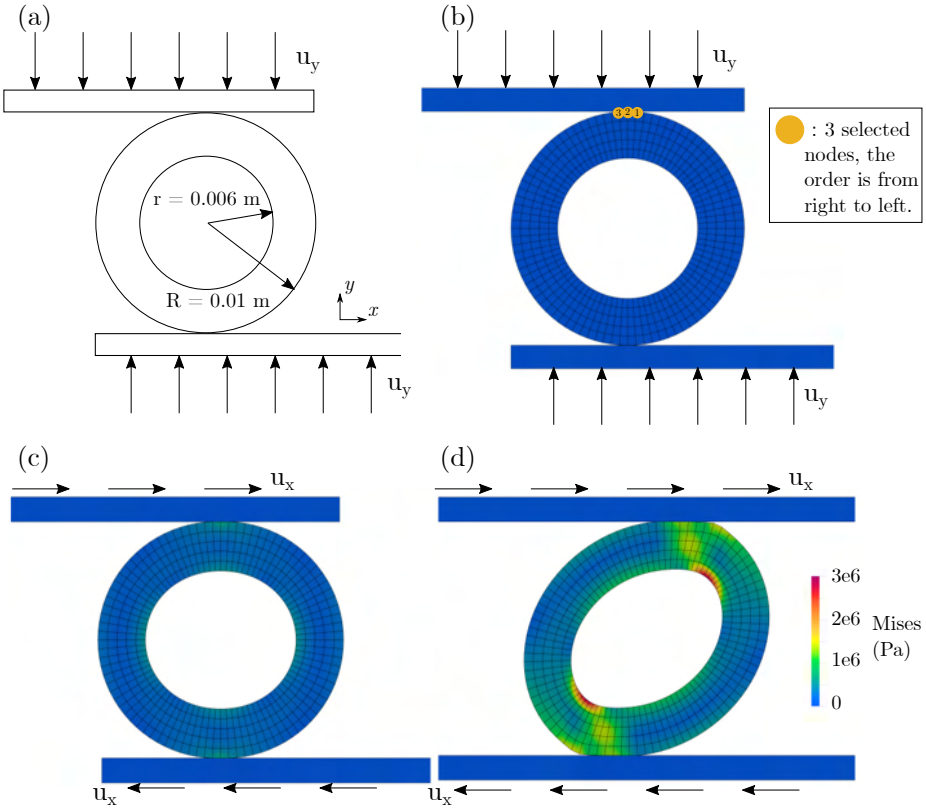

Figure 7: Rolling adhesion and friction of a confined hyperelastic wheel: (a) Problem setup; (b) The initial state of hyperelastic wheel; (c) Shape and Von Mises stress distribution of the confined wheel just before rotation; (d) Deformed shape and Von Mises stress distribution of the hyperelastic wheel during its rotation.

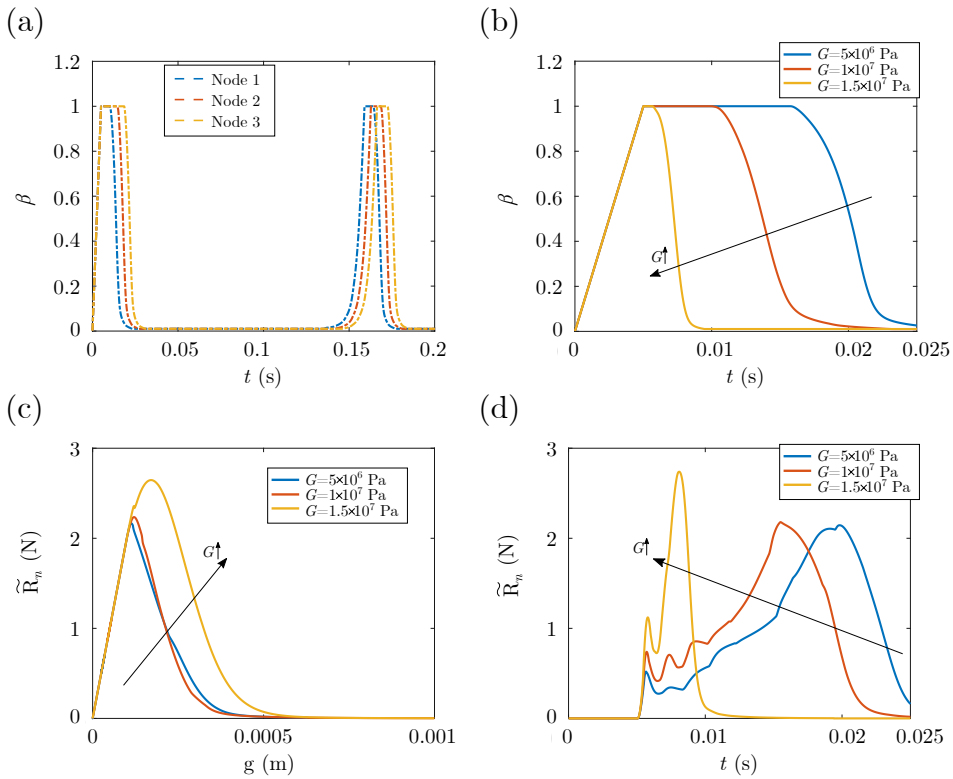

Figure 8: Rolling adhesion and friction of a confined hyperelastic wheel: (a) Evolution of β calculated on 3 selected nodes on the wheel surface. Locations of the 3 nodes are indicated in Figure 7(b). In this case, shear modulus $G = 1 \times 10^7$ Pa; (b) Evolution of β calculated on the first node with 3 sets of shear modulus ($G = 5 \times 10^6$ Pa, 1×10^7 Pa, and 1.5×10^7 Pa); (c) Traction-separation curves of the first selected node with 3 sets of shear modulus; (d) Evolution of the normal adhesion force $\tilde{R}_n$ with time on the first selected node under 3 sets of shear modulus G.

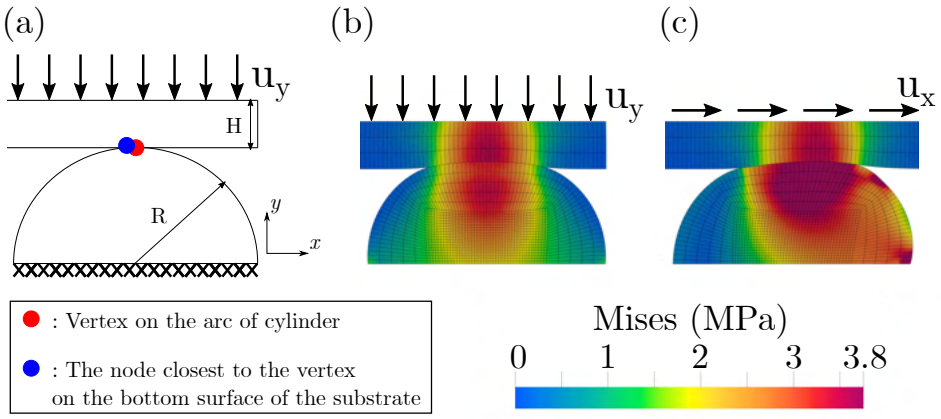

Figure 9: Adhesive friction between a hyperelastic plate and a deformable semi-cylinder: (a) Problem setup; (b) Distribution of Von Mises stress of the substrate and the cylinder at the end of push down; (c) Distribution of Von Mises stress at the end of calculation.

(a)

Case	1	2	3	4	5
Descent velocities (mm/s)	1000	500	333	250	200
Lateral velocites (mm/s)	1000	1000	1000	1000	1000

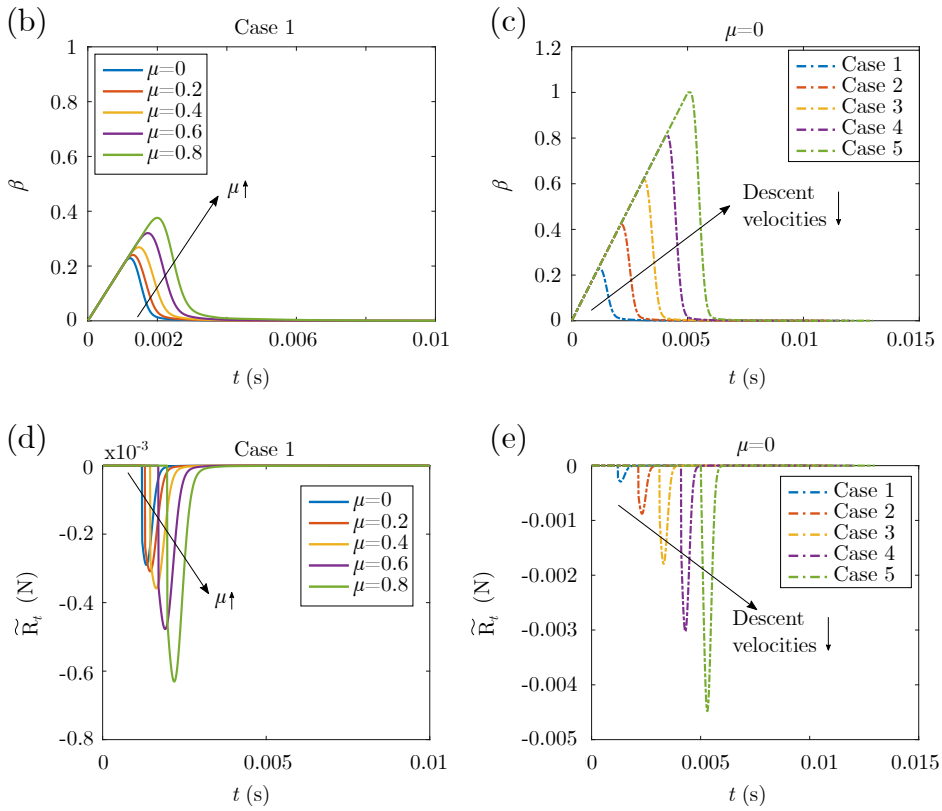

Figure 10: Adhesive friction between a hyperelastic plate and a deformable semi-cylinder: (a) 5 cases with different time and velocity of push down. This kind of setting is to ensure that the substrate has the same displacement during the whole process; (b) Evolution of β of blue node (see Figure 9(a)) with different friction coefficients μ in Case 1; (c) β evolution of blue node with different descent velocities under $\mu = 0$; (d) Evolution of the tangential adhesion force $\tilde{\mathrm{R}}_t$ of blue node with different friction coefficients μ in Case 1; (e) Evolution of the tangential adhesion force $\tilde{\mathrm{R}}_t$ of blue node with 5 cases under $\mu = 0$.

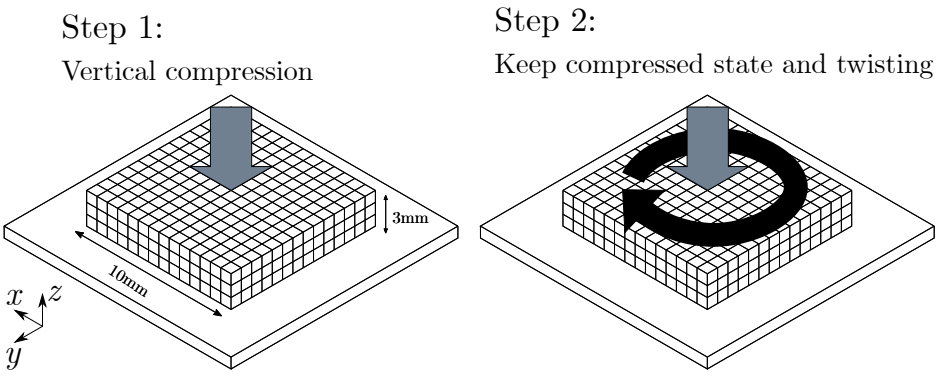

Figure 11: 3D adhesive frictional twisting: Problem setup and loading sequence (Step 1, compression and adhesion process; Step 2, twisting and de-bonding process)

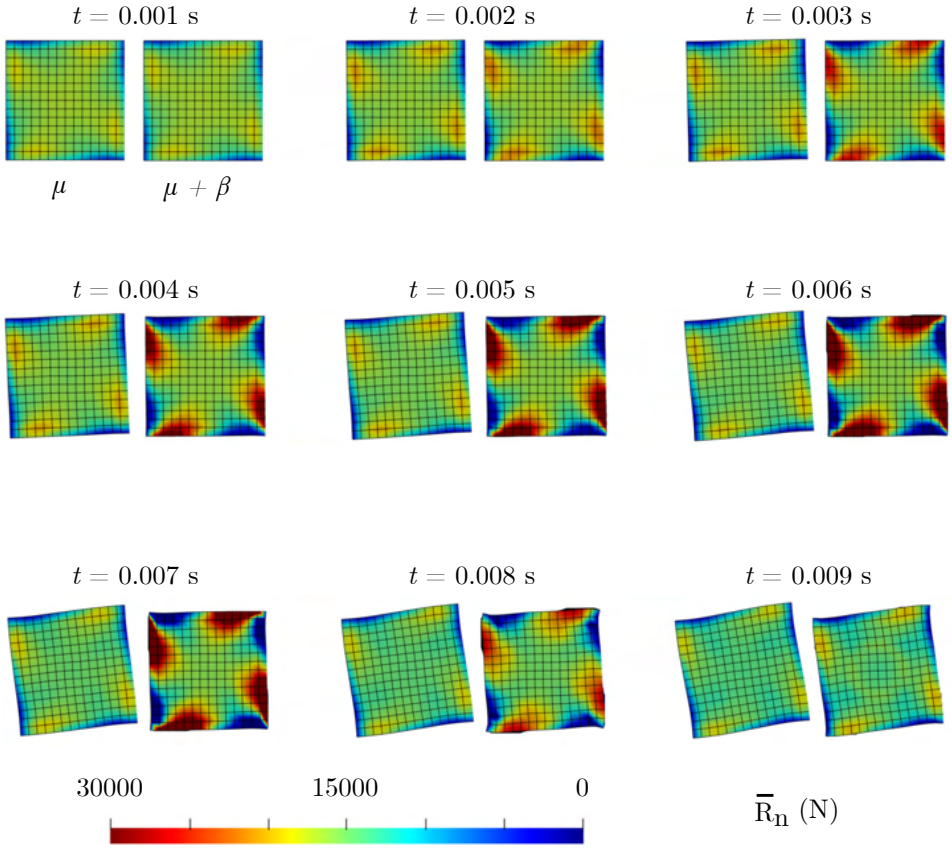

Figure 12: 3D adhesive frictional twisting: Evolution of the interface normal forces $\bar{\mathrm{R}}_n$ distribution during the twisting process. Comparison between dry friction (left) and adhesive friction (right) on each frame of time. For both cases, friction coefficient $\mu = 0.4$ is used.

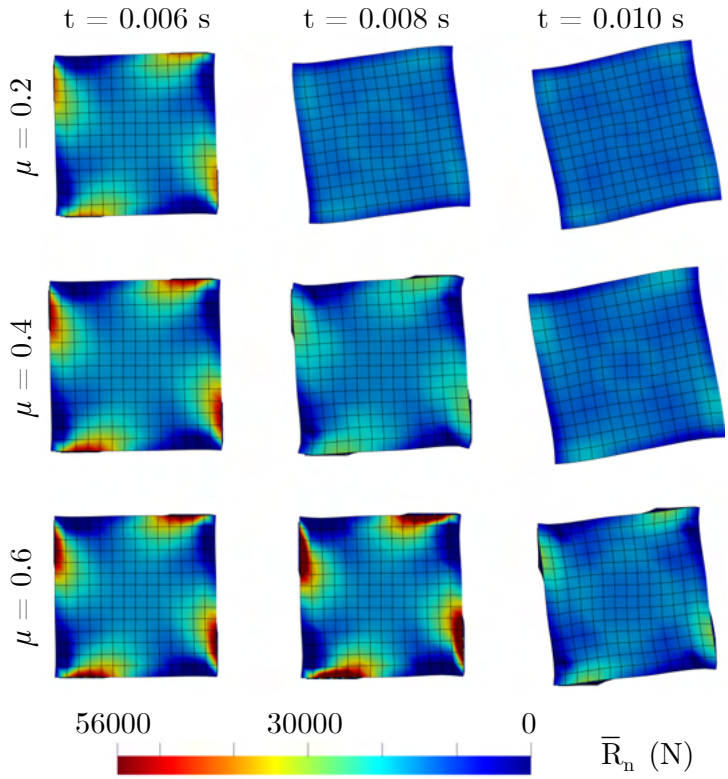

Figure 13: 3D adhesive frictional twisting: Influence of friction coefficient on the interface adhesive frictional behaviour. 3 sets of friction coefficients $\mu = 0.2$, 0.4 and 0.6 are considered.

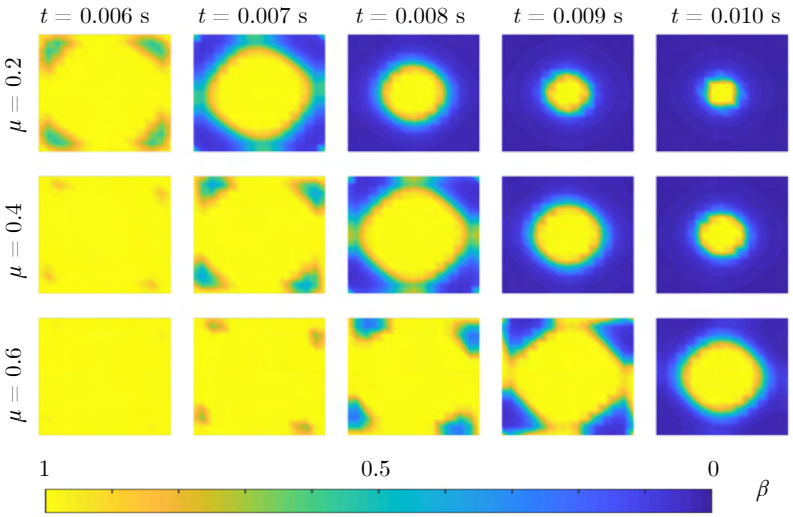

Figure 14: 3D adhesive frictional twisting: Evolution of the adhesion intensity during the twisting load, cacluated using 3 sets of friction coefficients $\mu = 0.2$, 0.4 and 0.6.

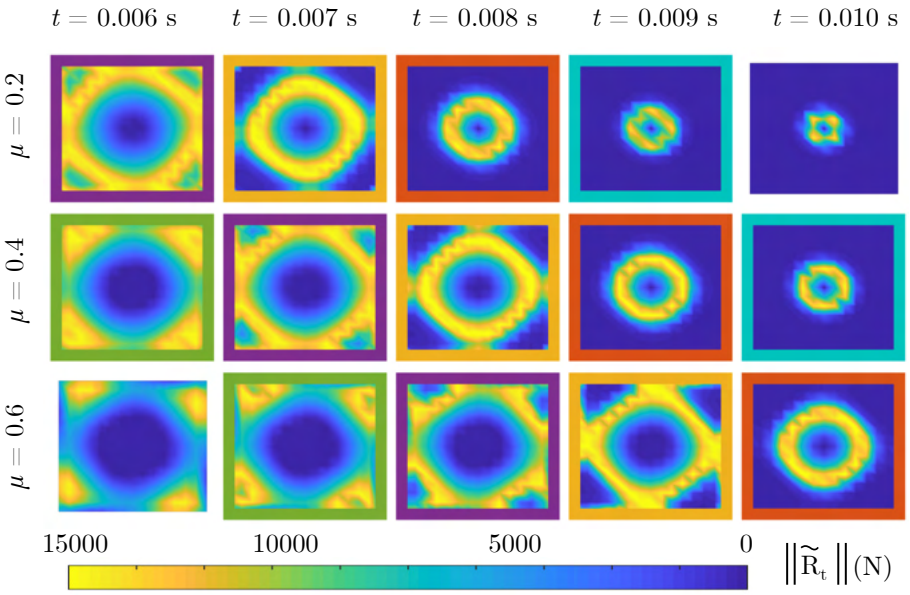

Figure 15: 3D adhesive frictional twisting: Evolution of tangential adhesion forces $\left\|\tilde{\mathrm{R}}_t\right\|$, calculated using 3 sets of friction coefficients $\mu = 0.2$, 0.4 and 0.6. The peak of tangential forces evolves as a circular band, whose radius reduces with time, before gradually disappearing in the centre of rotation, leading to complete de-bonding.

5 Conclusions

In this work, an extended 3D formulation for quasi-industrial problems of adhesive contact with recoverable interface between soft materials under large deformation is implemented by using the RCC interface model and the bi-potential resolution method. The RCC model proposes a straightforward description of the interface adhesion based on a local scalar parameter, and enables coupling the effect of adhesion, friction and unilateral contact within a unified framework. Both normal and tangential effects are taken into account by the adhesive interface model, involving both the process of bonding and de-bonding of the interface links. We have combined the 3D extended RCC adhesive interface model with 3D Blatz-Ko hyperelasticity to account for frictional contact of foam type soft material structures with recoverable interface under conditions of large deformation. To illustrate the ability of the implemented model to deal with real problems, we have treated various 3D test cases involving normal, tangential, and mixed-directional scenarios of adhesive contact with/without adhesion recoverability, which is very close to quasi-industrial modelling situations. Future extensions of this work include, for example, the account for anisotropic interface behaviours and the effect of interface fatigue which is a common phenomenon in adhesive applications involving cyclic loads.

Acknowledgement

We gratefully acknowledge the financial support of the National Natural Science Foundation of China (Grant No. 11772274).

References

[1] K. Autumn and J. Puthoff. Properties, principles, and parameters of the gecko adhesive system. In Andrew M. Smith, editor, *Biological Adhesives*, pages 245–280. Springer International Publishing, Cham, 2016.

[2] D. Labonte, C. J. Clemente, A. Dittrich, C.-Y. Kuo, A. J. Crosby, D. J. Irschick, and W. Federle. Extreme positive allometry of animal adhesive pads and the size limits of adhesion-based climbing. *Proceedings of the National Academy of Sciences*, 113(5):1297–1302, 2016.

[3] C. Cerutti and A. J. Ridley. Endothelial cell-cell adhesion and signaling. *Experimental Cell Research*, 358(1):31–38, 2017.

[4] S. Di Cio and J. E. Gautrot. Cell sensing of physical properties at the nanoscale: Mechanisms and control of cell adhesion and phenotype. *Acta Biomaterialia*, 30:26–48, 2016.

[5] L. Afferrante and G. Carbone. The ultratough peeling of elastic tapes from viscoelastic substrates. *Journal of the Mechanics and Physics of Solids*, 96:223–234, 2016.

[6] G. Carbone, E. Pierro, and S. N. Gorb. Origin of the superior adhesive performance of mushroom-shaped microstructured surfaces. *Soft Matter*, 7(12):5545, 2011.

[7] S. Das, N. Cadirov, S. Chary, Y. Kaufman, J. Hogan, K. L. Turner, and J. N. Israelachvili. Stick-slip friction of gecko-mimetic flaps on smooth and rough surfaces. *Journal of The Royal Society Interface*, 12(104):20141346, 2015.

[8] L. Xue, J. T. Pham, J. Iturri, and A. del Campo. Stick–slip friction of pdms surfaces for bioinspired adhesives. *Langmuir*, 32(10):2428–2435, 2016.

[9] M. Bazrafshan, M. B. de Rooij, and D. J. Schipper. On the role of adhesion and roughness in stick-slip transition at the contact of two bodies: A numerical study. *Tribology International*, 121:381–388, 2018.

[10] D. Liprandi, F. Bosia, and N. M. Pugno. A theoretical-numerical model for the peeling of elastic membranes. *Journal of the Mechanics and Physics of Solids*, 136:103733, 2020.

[11] J. C. Mergel, R. Sahli, J. Scheibert, and R. A. Sauer. Continuum contact models for coupled adhesion and friction. *The Journal of Adhesion*, 95(12):1101–1133, 2019.

[12] M. Cocou, M. Schryve, and M. Raous. A dynamic unilateral contact problem with adhesion and friction in viscoelasticity. *Zeitschrift für Angewandte Mathematik und Physik*, 61(4):721–743, 2010.

[13] M. K. Salehani, N. Irani, and L. Nicola. Modeling adhesive contacts under mixed-mode loading. *Journal of the Mechanics and Physics of Solids*, 130:320–329, 2019.

[14] K. Langstreth Johnson, K. Kendall, A. D. Roberts, and D. Tabor. Surface energy and the contact of elastic solids. *Proceedings of the Royal Society of London. A. Mathematical and Physical Sciences*, 324(1558):301–313, 1971.

[15] D. Maugis. Adhesion of spheres: The JKR-DMT transition using a Dugdale model. *Journal of Colloid and Interface Science*, 150(1):243–269, 1992.

[16] J. A. Greenwood and K. L. Johnson. The mechanics of adhesion of viscoelastic solids. *Philosophical Magazine A*, 43(3):697–711, 1981.

[17] G.-Y. Huang and J.-F. Yan. A mechanical model for the adhesive contact with local sliding induced by a tangential force. *Acta Mechanica Solida Sinica*, 30(4):369–373, 2017.

[18] J. C. Mergel, J. Scheibert, and R. A. Sauer. Contact with coupled adhesion and friction: Computational framework, applications, and new insights. *Journal of the Mechanics and Physics of Solids*, 146:104194, 2021.

[19] M. Raous. Quasistatic Signorini problem with Coulomb friction and coupling to adhesion. In P. Wriggers and P. Panagiotopoulos, editors, *New Developments in Contact Problems, CISM Courses and Lectures, n°384*, pages 101–178. Springer Vienna, Vienna, 1999.

[20] M. Raous. Friction and adhesion. In P. Alart, P. Maisonneuve, and R.T. Rockafellar, editors, *Advances in Mechanics and Mathematics*, pages 93–105. Kluwer Academic Publishers, 2006.

[21] M. Raous. Interface models coupling adhesion and friction. *Comptes Rendus Mécanique*, 339(7):491–501, 2011.

[22] M. Raous, L. Cangémi, and M. Cocu. A consistent model coupling adhesion, friction, and unilateral contact. *Computer Methods in Applied Mechanics and Engineering*, 177(3-4):383–399, 1999.

[23] M. Fremond. Contact with adhesion. In *Nonsmooth Mechanics and Applications*, pages 177–221. Springer Vienna, 1988.

[24] M. Raous, M. Schryve, and M. Cocou. Recoverable adhesion and friction. In C.C. Banagiotopoulos, editor, *Nonsmooth/Nonconvex Mechanics with applications in Engineering*, pages 165–172. Ziti Publisher, 2006.

[25] G. Del Piero and M. Raous. A unified model for adhesive interfaces with damage, viscosity, and friction. *European Journal of Mechanics - A/Solids*, 29(4):496–507, 2010.

[26] B. Halphen and Q. Nguyen. Sur les matériaux standard généralisés. *Journal de Mécanique*, 14:39–63, 01 1975.

[27] D. G. Luenberger and Y. Ye. Penalty and barrier methods. In D. G. Luenberger and Y. Ye, editors, *Linear and Nonlinear Programming*, pages 397–428. Springer International Publishing, 2016.

[28] D. P. Bertsekas. *Constrained Optimization and Lagrange Multiplier Methods*. Academic Press, 1982.

[29] P. Alart and A. Curnier. A mixed formulation for frictional contact problems prone to Newton like solution methods. *Computer Methods in Applied Mechanics and Engineering*, 92(3):353–375, 1991.

[30] J. C. Simo and T. A. Laursen. An augmented Lagrangian treatment of contact problems involving friction. *Computers & Structures*, 42(1):97–116, 1992.

[31] G. de Saxcé and Z.-Q. Feng. New inequality and functional for contact with friction: The implicit standard material approach. *Mechanics of Structures and Machines*, 19(3):301–325, 1991.

[32] G. de Saxcé and Z.-Q. Feng. The bipotential method: A constructive approach to design the complete contact law with friction and improved numerical algorithms. *Mathematical and Computer Modelling*, 28(4-8):225–245, 1998.

[33] Z.-Q. Feng, M. Zei, and P. Joli. An elasto-plastic contact model applied to nanoindentation. *Computational Materials Science*, 38(4):807–813, 2007.

[34] L. Peng, Z.-Q. Feng, P. Joli, J.-H. Liu, and Y.-J. Zhou. Automatic contact detection between rope fibers. *Computers & Structures*, 218:82–93, 2019.

[35] Y.-J. Zhou, Z.-Q. Feng, J. A. R. Quintero, and P. Ning. A computational strategy for the modeling of elasto-plastic materials under impact loadings. *Finite Elements in Analysis and Design*, 142:42–50, 2018.

[36] P. Ning, Z.-Q. Feng, J. A. R. Quintero, Y.-J. Zhou, and L. Peng. Uzawa algorithm to solve elastic and elastic–plastic fretting wear problems within the bipotential framework. *Computational Mechanics*, 62(6):1327–1341, 2018.

[37] P. Ning, Y. Li, and Z.-Q. Feng. A Newton-like algorithm to solve contact and wear problems with pressure-dependent friction coefficients. *Communications in Nonlinear Science and Numerical Simulation*, 85:105216, 2020.

[38] N. Terfaya, A. Berga, and M. Raous. A bipotential method coupling contact, friction and adhesion. *International Review of Mechanical Engineering*, 9(4):341–352, 2015.

[39] P. J. Blatz and W. L. Ko. Application of finite elastic theory to the deformation of rubbery materials. *Transactions of the Society of Rheology*, 6(1):223–252, 1962.

[40] P. G. Ciarlet and J. Nečas. Unilateral problems in nonlinear, three-dimensional elasticity. *Archive for Rational Mechanics and Analysis*, 87(4):319–338, 1985.

[41] M. Jean. The non-smooth contact dynamics method. *Computer Methods in Applied Mechanics and Engineering*, 177(3):235–257, 1999.

[42] M. Raous and Y. Monerie. Unilateral contact, friction and adhesion: 3D cracks in composite materials. In J.A.C. Martins and M.D.P. Monteiro Marques, editors, *Contact Mechanics*, pages 333–346. Kluwer, 2002.

[43] K. K. Tamma and R. R. Namburu. A robust self-starting explicit computational methodology for structural dynamic applications: Architecture and representations. *International Journal for Numerical Methods in Engineering*, 29(7):1441–1454, 1990.

[44] Z.-Q. Feng. 2D or 3D frictional contact algorithms and applications in a large deformation context. *Communications in Numerical Methods in Engineering*, 11(5):409–416, 1995.

A bi-potential contact formulation for recoverable adhesion between soft bodies based on the RCC interface model

1 Supplementary information

According to Eq.(16), β significantly decreases during the process of debonding. It tends towards zero but never exactly reaches zero. For reasons of practice, it is convenient to introduce a limit value of β, denoted by ε, that indicates complete debonding between the adhesive contact surfaces. Therefore with $\beta < \varepsilon$, we can consider that the adhesion bonds are completely broken. In this work, we adopt an empirical value of $\varepsilon = 10^{-4}$ for which adhesion forces drop to the 10^{-9} magnitude. An example depicting the evolution of β during debonding is provided here, based on the test case illustrated in Section 4.3. We focus on the phase of separation between the soft semi-cylinder that slides on the rigid plate with adhesive interface.

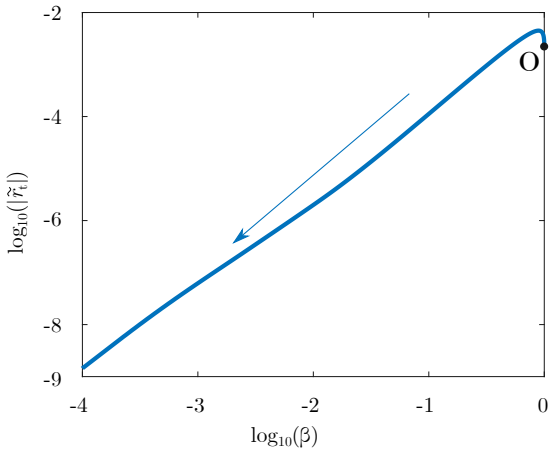

Figure 1: Evolution of adhesion forces as function of β on logarithmic scale: with β on the order of 10^{-4}, adhesion forces become negligible on the 10^{-9} order.

Figure 1 shows the evolution of adhesion forces as function of β on logarithmic scale. Starting from Point O, adhesion force first increases with the gap between contact surfaces, then due to the surface debonding, very quickly drops to insignificant levels. With β on the order of 10^{-4}, we observe negligible adhesion forces on the 10^{-9} order.